Chapter 7

AMR Sensor and its Application on Nondestructive Evaluation

Dongfeng He

Additional information is available at the end of the chapter

http://dx.doi.org/10.5772/intechopen.70334

Abstract

To improve the performance of anisotropic magnetoresistance (AMR) sensor, a low-noise driving circuit for the AMR sensor was developed and the magnetic field noise spectral densities of 12 pT/root(Hz) at 1 kHz and 20 pT/root(Hz) at 100 Hz were achieved. The driving circuit could operate in amplifier mode or feedback mode. For the driving circuit with feedback, the distortion of the system was reduced and the AMR sensor was suitable for the applications in the environment without shielding. The Set/Reset method was used to reduce the low frequency noise of the AMR sensor. Due to the low noise of AMR sensor, the eddy current testing (ECT) system with the AMR sensor had the advantage of detecting deep and small defects in metal structures. The dual frequency ECT system was developed to reduce the influence of lift-off variance. Using the ECT system with the AMR sensor, we successfully detected the small defects in the combustion chamber of liquid rocket.

Keywords: AMR (anisotropic magneto-resistance) sensor, NDE (nondestructive evaluation), ECT (eddy current testing), driving circuit, defect, combustion chamber

1. Introduction

Eddy current testing (ECT) is an effective nondestructive evaluation (NDE) method to detect defects in metal (or conductive) structures. For the ECT NDE method, alternating magnetic field is produced when alternating current (AC) current flows in the excitation coil; so eddy current is induced in the conductive sample and the defect in the sample changes the amplitude and the distribution of the eddy current. By measuring the change of the eddy current, the defect can be detected.

Many magnetic sensors have been used to construct ECT NDE systems, such as inductive coil [1], hall sensor [2], giant magnetoresistive (GMR) sensor [3, 4], anisotropic magnetoresistance

(AMR) sensor [5, 6], flux gate [7, 8] and superconducting quantum interference device (SQUID) [9–11]. Compared with other sensors, SQUID has the lowest noise, but it needs liquid nitrogen or liquid helium for the cooling, which is not convenient for some industrial applications. Stutzke et al. [12] measured the noise spectral densities in the frequency range from 0.1 Hz to 10 kHz on a variety of commercially available magnetic sensors of GMR sensors, AMR sensors and tunnel magnetoresistance (TMR) sensors. The results show that AMR sensor had the lowest magnetic field noise spectrum density with the order of 100 pT/root(Hz) in the frequency range from 1 Hz to 1 kHz. And we also achieved much better performances by optimizing the driving circuit of the AMR sensor [13], so we chose AMR sensor to construct our ECT NDE systems.

In this chapter, we will summarize our research on AMR sensor and its application on ECT NDE. Firstly, we will give an introduction of AMR sensor; secondly, describe the optimization of the AMR sensor: lowering the noise, feedback operation and reducing the temperature effect using Set/Reset method; then, the application of AMR sensor to NDE for the defect detection of the combustion chamber of liquid rocket; finally, the conclusion.

The AMR effect was first discovered in 1857 by Thomson [14]. Different from the ordinary magneto-resistive effect in metals, the AMR effect appeared in ferromagnetic materials [15], which was explained as the spin-orbit interaction. In this effect, the resistivity depended on the orientation of magnetization with respect to the direction of the electric current. The change of the longitudinal resistivity of the material magnetized parallel to the current direction was larger than that of the transverse resistivity of the material magnetized perpendicular to the current direction [15]. In the absence of the external magnetic field, the direction of the magnetization was along the anisotropy axis (the so-called easy axis). To change the direction of the magnetization, the applied magnetic field should be perpendicular to the anisotropy axis, so the direction perpendicular to the anisotropy axis was called the sensitive axis. The thin film of the NiFe alloy (permalloy) was most frequently used for preparing AMR sensors. **Figure 1** shows the typical magnetoresistive coefficient ΔR/R for a thin film permalloy magnetoresistor.

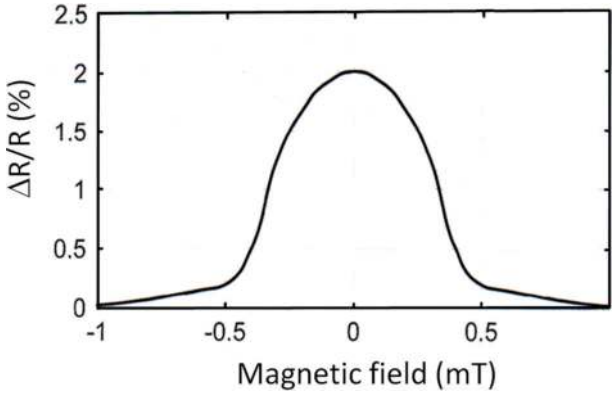

Figure 1. Typical magnetoresistive coefficient of an AMR thin film permalloy magnetoresistor.

To obtain the linear characteristics of an AMR sensor, the current path should be 45° inclined to the anisotropy axis [16], as shown in **Figure 2**.

The resistive Wheatstone bridge was often used to construct the AMR sensor, such as the HMC1001 of Honeywell [17]. For the AMR sensor with Wheatstone bridge, it only required a supply voltage to bias the sensor. **Figure 3(a)** shows the Wheatstone bridge element of an AMR sensor. The sensitive directions of magnetoresistor 1 and 3 were opposite to the sensitive directions of magnetoresistor 2 and 4. For some commercial AMR sensors, Offset straps and Set/Reset straps were often integrated with the AMR sensor chips. **Figure 3(b)** shows it.

The Offset strap was a spiral of metallization that coupled to the sensor element's sensitive axis. Using the Offset strap, the unwanted signal could be compensated, such as the offset voltage of the bridge and the DC magnetic field. Another advantage of the Offset strap was that it could be used to construct the feedback circuit of the AMR sensor and the distortion of output signal could be reduced.

When AMR sensor was exposed in a strong magnetic field (>4–20 Gauss), which could demagnetize the AMR sensor [18], the AMR effect was reduced and the sensitivity of the AMR sensor could be significantly reduced. To recover the sensitivity of the AMR sensor, the Set/Reset

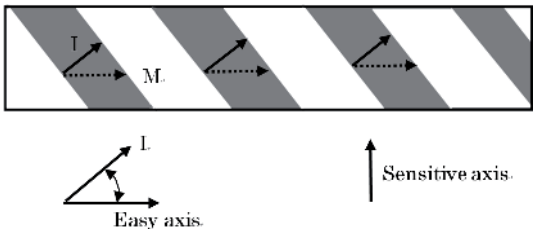

Figure 2. AMR sensor with the inclination of the current path by the angel 45° to the easy axis.

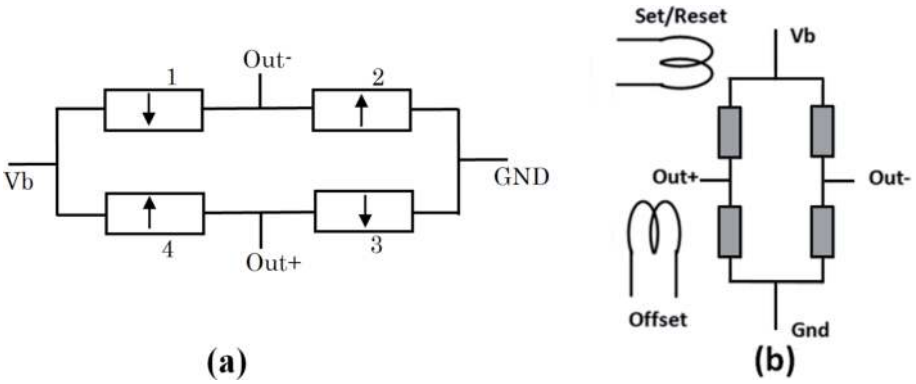

Figure 3. (a) Magnetoresistive Wheatstone bridge elements of AMR sensor. (b) The construction of AMR sensor with Offset strap and Set/Reset strap.

strap was used, which was another spiral of metallization that coupled to the sensor element's easy axis (perpendicular to the sensitive axis on the sensor die). When a high current pulse was applied to the Set/Reset strap, the magnetization of the AMR sensor was recovered and the AMR sensor was Set/Reset to high sensitivity. The sensitive direction was reversed when the reset current direction was opposite. Using the Set/Reset strap, we developed a reversal bias method to reduce the influence of temperature drift to the AMR sensor, which will be described in Section 2.

Table 1 shows the typical performance data of the HMC1001 AMR sensor of Honeywell. To understand the properties of the sensor, we give some explanations about the specifications of the AMR sensor. The sensitivity (S) of a magnetic sensor means the output voltage of the sensor when one Gauss magnetic field is applied. The typical sensitivity of the AMR sensor HMC1001 is 3.2 mV/V/Gauss. For the AMR sensor, the sensitivity has relation with the bias voltage. If the bias voltage is 5 V, the sensitivity is 3.2 × 5 = 16 mV/Gauss; if the bias voltage is 10 V, the sensitivity is 3.2 × 10 = 32 mV/Gauss.

For an AMR sensor with driving circuit, the signal is amplified (amplifier mode) or changed (feedback mode). We use field/voltage transfer coefficient ($\Delta B/\Delta V$) to express it, which means the corresponding magnetic field for 1 V output signal. For a sensor works in amplifier mode, if the total gain of the amplifier is G, we have $\Delta B/\Delta V = G/S$.

Using spectrum analyzer, we can measure the output voltage noise spectral density V_n of the sensor. Then we can get the magnetic field noise spectral density $B_n = V_n*(\Delta B/\Delta V)$.

Bridge supply voltage (V)	5
Resistance (Ω)	600–1200
Sensitivity (mV/V/Gauss)	3.2
Field range (Gauss)	−2~2
Operating temperature (°C)	−55 to 150
Linearity error at ±1 Gauss (%FS)	0.1
Linearity error at ±2 Gauss (%FS)	1
Equivalent input voltage noise density at 1 Hz (nv/√Hz)	29
Bridge offset (mv)	−60 to 30
Magnetic field noise by 10 Hz bandwidth (μGauss)	27*
Set/Reset Current (A)	2~5
Offset temperature drift without Set/Reset (%/°C)	±0.03
Offset temperature drift with Set/Reset (%/°C)	±0.001
Offset constant (mA/Gauss)	51
Bandwidth (MHz)	5

*27 is the root mean square (RMS) value.

Table 1. The specifications of the AMR sensor HMC1001 [17].

V_n has relation to the gain of the driving circuit, but B_n has no relation to the gain of the driving circuit. B_n is more commonly used to express the characteristics of a magnetic sensor. If the signal bandwidth is Δf, then the magnetic resolution is $B_n*(\Delta f)^{1/2}$. If Δf is 1 Hz, the magnetic field resolution is equal to B_n, so sometimes, we also call B_n the magnetic field resolution.

Due to its small size, low cost and high sensitivity, anisotropic magnetoresistance (AMR) sensor has been used for many applications, such as navigation, nondestructive evaluation (NDE) and vehicle detection. To improve the performance of the AMR sensor, we optimized the driving circuit of the AMR sensor. Lower noise was obtained. The distortion was reduced using feedback method, and the influence of temperature fluctuation was reduced using Set/Reset method.

2. Optimization of the AMR sensor: low noise, feedback and Set/Reset

We developed a low noise driving circuit for the AMR sensor. **Figure 4** shows the block diagram of the circuit. The driving circuit could operate in amplifier mode or feedback mode [13]. We used a voltage source to bias the AMR sensor. The output of the Wheatstone bridge of the AMR sensor was sent to a differential preamplifier made by low noise operational amplifier of LT1028. The total gain of the preamplifier and the amplifier was 500. The switch SW1 was used to change the operation mode. If SW1 was turned to OFF, it was in amplifier mode, and the output of the amplifier V_{amp} measured the magnetic field. If SW1 was turned to ON, the circuit was in feedback mode. For the feedback mode, an integrator and a feedback resistance R_f were used. Through the feedback resistance R_f, the feedback current was sent to the Offset strap of HMC1001, the signal of V_{out} measured the magnetic field.

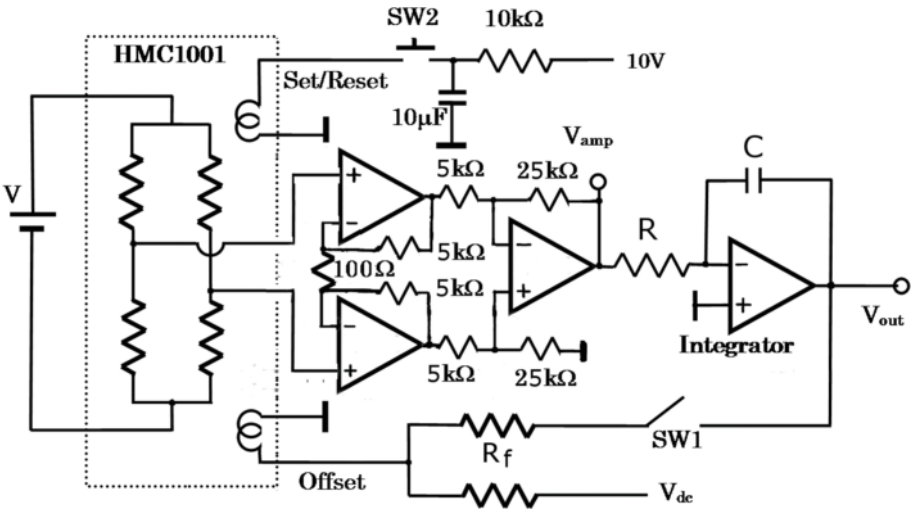

Figure 4. Block diagram of the driving circuit for AMR sensor.

The response bandwidth of the driving circuit was determined by the feedback resistance R_f, the resistance R and the capacitor C of the integrator. When R_f of 500 Ω, R of 2 kΩ and C of 220 pF were used, the response bandwidth was about 300 kHz. The offset magnetic field was adjusted by the DC voltage of V_{dc}. When the driving circuit of AMR sensor operated in feedback mode, the operation point was locked to a fixed point, thus, the distortion of the output signal was reduced.

To restore the high sensitivity of the AMR sensor, a simple Set/Reset method was used in our circuit. When the switch SW2 was OFF, the capacitor of 10 μF was charged to 10 V through the resistance of 10 kΩ. When switch SW2 was momentarily closed, a Set pulse with current amplitude of about 4 A was produced to restore the AMR sensor.

The sensitivity of the AMR sensor was proportional to the bias voltage. From the data sheet of HMC1001, the typical bias voltage was 5V and the maximum bias voltage was about 12 V. Our experiments proved that the bias voltage could be increased to 24 V and the AMR sensor still was not damaged. There were three contributions to the total noise of the AMR sensor: the noise produced by the driving circuit; the thermal noise of the resistance of the bridge; and the intrinsic magnetic noise of the AMR sensor itself. **Figure 5** shows the equivalent input voltage noise spectral density for different bias voltages from 4 to 24 V. The noise spectral density was measured when the driving circuit was at amplifier mode. For higher frequency (above 1 kHz), the thermal noise of the bridge had a big contribution to the total noise. The white noise increased a little bit for higher bias voltage. The reason was that the temperature

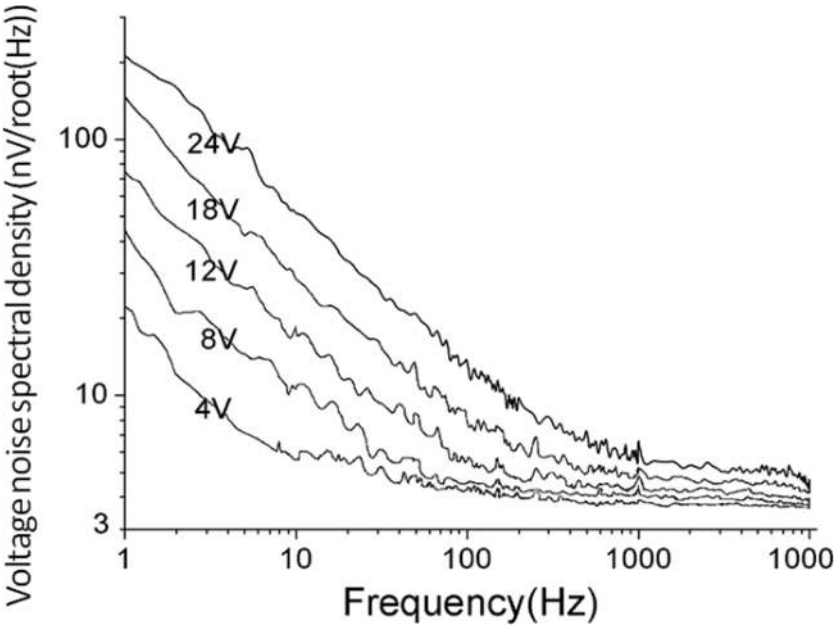

Figure 5. The equivalent input voltage noise spectral density for the bias voltage from 4 to 24 V.

of the sensor chip was increased with higher bias voltage. For lower frequency, the noise of the AMR sensor was mainly determined by the intrinsic magnetic noise of the AMR sensor, which might be caused by the random movement of the magnetic domain in the sensor film.

When the driving circuit was in feedback mode, to calibrate the AMR sensor's output, a 10 turn circular coil with a diameter of 50 cm was used to produce a magnetic field when an AC current of 230 Hz was applied to the coil. A Gauss meter and the AMR sensor were put in the center of the coil to measure the magnetic field. After calibration, the transfer coefficient of the magnetic field and the output voltage of the AMR sensor ($\Delta B/\Delta V$) was about 0.039 Gauss/V. Now, we made a simple estimation of the transfer coefficient. Since the feedback resistance was 500 Ω, the feedback current for 1 V output was 1000/500 = 2 mA/1V. Considering the offset constant (**Table 1**) was about 51 mA/Gauss, we could calculate the transfer coefficient 2/51 = 0.0392 Gauss/V, which was very close to the measured value of 0.039 Gauss/V. **Figure 6** shows the magnetic field noise spectral density of the AMR sensor for different bias voltages. The measurement was done in a magnetic shielding room. The low frequency magnetic field noise spectral densities were almost same for all bias voltages. The reason was that the intrinsic magnetic noise of the AMR sensor determined the total noise. At high frequency, the AMR sensor had lower magnetic noise spectral density when bigger bias voltage was used. When the AMR sensor had the bias voltage of 24 V, the magnetic field noise spectral densities were about 12 pT/root(Hz) at 1 kHz and 20 pT/root(Hz) at 100 Hz. These values

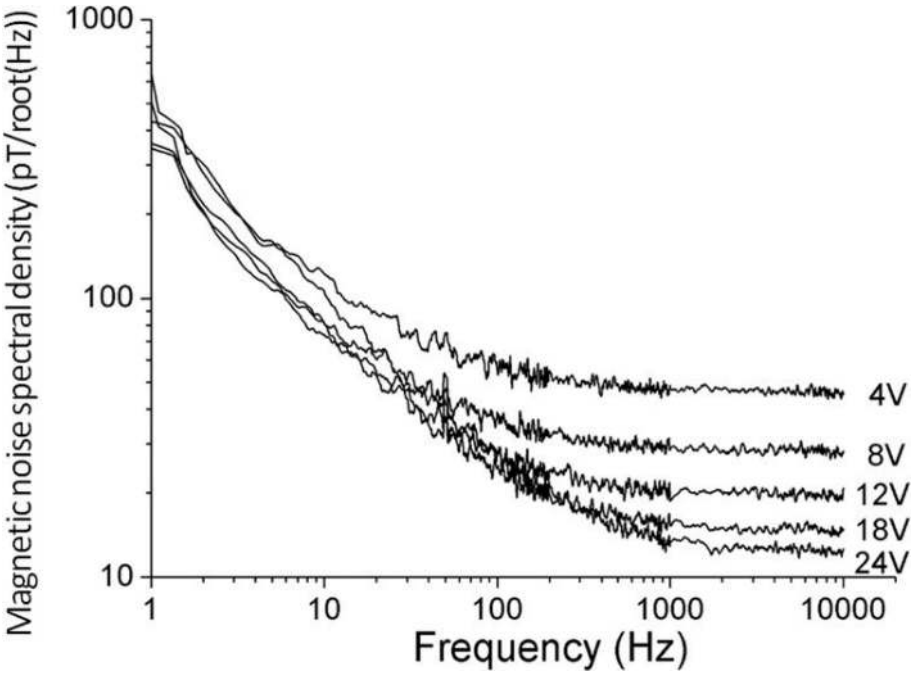

Figure 6. The magnetic field resolution of AMR sensor.

were obtained when the driving circuit was at feedback mode. We could estimate it using the sensitivity and the equivalent input noise spectral density of the AMR sensor. When the bias voltage was 24 V, the sensitivity of the AMR sensor was about 3.2 × 24 = 76.8 mV/Gauss = 0.768 nV/pT. From **Figure 5**, the equivalent input voltage noise spectral density was about 7 nV/root(Hz) at 1 kHz; then we could estimate the magnetic field noise spectrum was about 7/0.768 = 9 pT/√Hz, which was close to the measured value of 12 pT/√Hz.

When AMR sensor was biased by a voltage, the power produced by the AMR sensor made the temperature of the AMR sensor higher than environmental temperature. When a sample was close to the AMR sensor, it caused a small thermal disturbance and the AMR sensor had a signal output. We observed this phenomenon [19] and developed a method to reduce the influence of this heat transfer effect [20].

Figure 7 shows the setup of the experiment. A small platinum resistance of FK222-1000-A with the size of 2.3 × 2.1 × 0.8 mm^3 was used as the temperature sensor and it was tightly glued to one side of the AMR sensor. Due to its small size, it had small influence to the temperature of the AMR sensor. The resistance of the Pt resistor was 1000 Ω at 0°C, the temperature coefficient was about 3850 ppm/K, and the temperature resolution was about 0.15°C. A DC current of 0.1 mA was used to bias the Pt resistor, and the voltage across the Pt resistor was amplified by an amplifier with the gain of 40 dB. The sample was fixed on the X-Y stage for the scanning. A computer was used to control the movement of the X-Y stage and to make the data acquisition and the data procession.

Figure 8 shows the temperature of the AMR sensor with different bias voltages from 0 to 33.4 V (a correction to [19], the bias voltage in [19] should be 2 times). For higher bias voltage, the thermal power of the AMR sensor was also bigger, so the temperature of the AMR sensor increased with the bias voltage. The temperature was 22.5°C in our laboratory. When

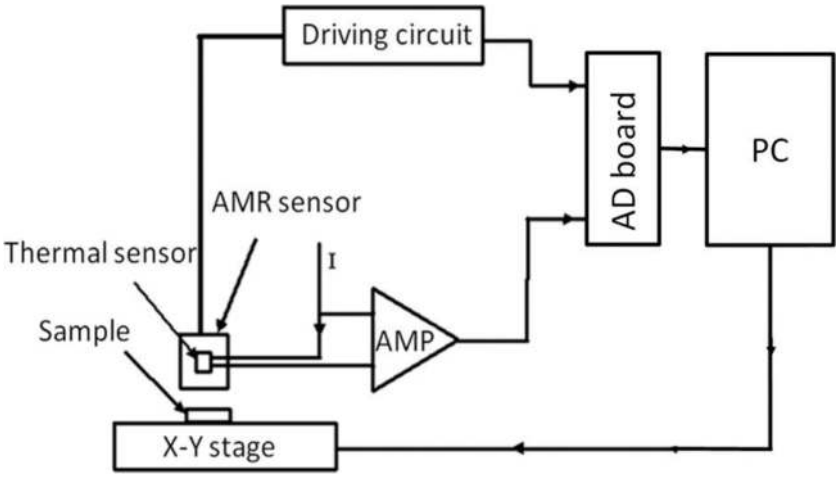

Figure 7. The experimental setup of simultaneously monitoring the temperature and the signal output of the AMR sensor.

http://dx.doi.org/10.5772/intechopen.70334

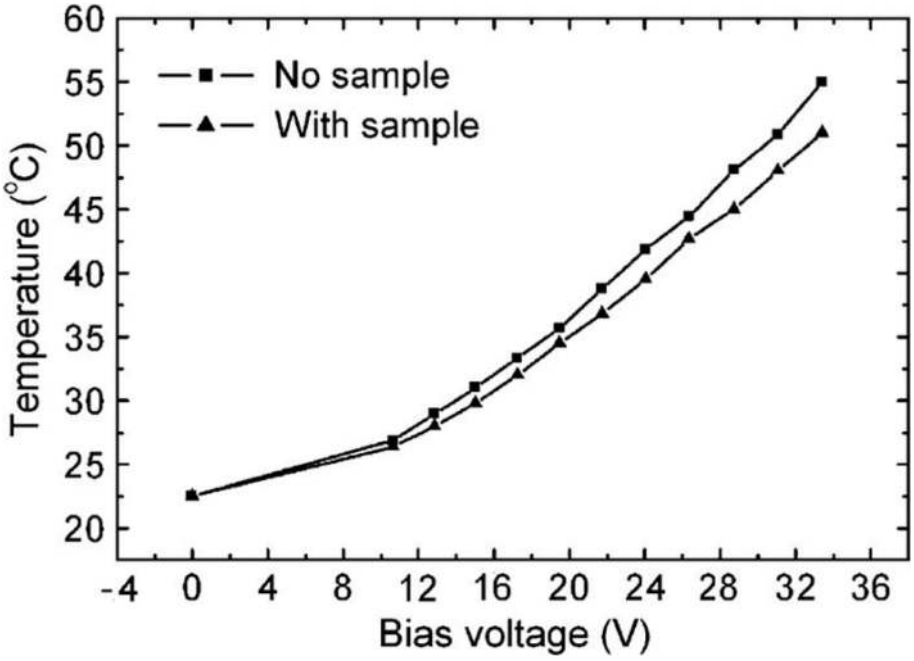

Figure 8. Temperature of the AMR sensor versus the bias voltage.

there was no sample, the temperature of the AMR sensor was about 42°C for the bias voltage of 24 V; when a 15 × 15 × 1 mm^3 copper plate was put under the AMR sensor with the lift-off distance of 0.2 mm, the temperature of the AMR sensor decreased to about 39.5°C.

For the AMR sensor of HMC1001, the temperature fluctuation causes the changes of the sensitivity, the resistance and the bridge offset, so the output signal of the AMR sensor also changes with the temperature of the AMR sensor. To measure the temperature fluctuation and the signal output of the AMR sensor correctly, we put a small copper plate with the size of about 15 × 15 × 1 mm^3 on the X-Y stage for the scanning. The lift-off distance between the AMR sensor and the copper plate was about 0.2 mm. The bias voltage of the AMR sensor was 24 V. The curves of (a) and (b) in **Figure 9** show the output signal and the temperature change of the AMR sensor when the copper plate was moved close to the AMR sensor. The two curves were very consistent, which proved that the output signal change of the AMR sensor was caused by the temperature fluctuation.

To reduce the influence of temperature drift and the heat transfer effect of AMR sensor, we developed a driving circuit for the AMR sensor with the Set/Reset method. **Figure 10** shows the block diagram. **Figure 11** shows the waveforms of the testing points in **Figure 10**. In our AMR sensor system, a square wave generator was used to produce a square wave with the frequency of about 20 kHz, which was the waveform 1 shown in **Figure 11**. After a power amplifier, a capacitor of 0.2 μF was used to produce the pulse to Set/Reset the AMR sensor.

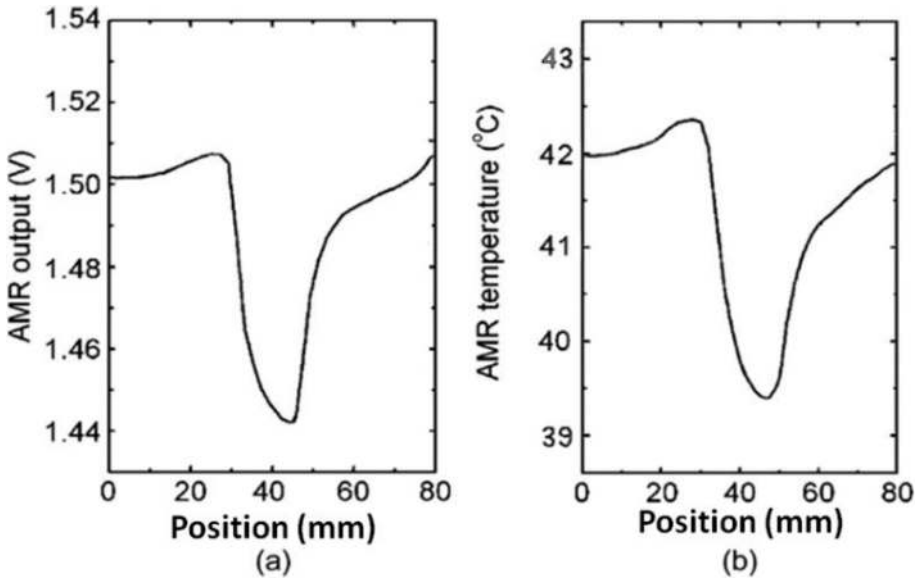

Figure 9. (a) Signal output of AMR sensor when a copper plate was close to the sensor. (b) Temperature change of the AMR sensor when the copper plate was close to the sensor.

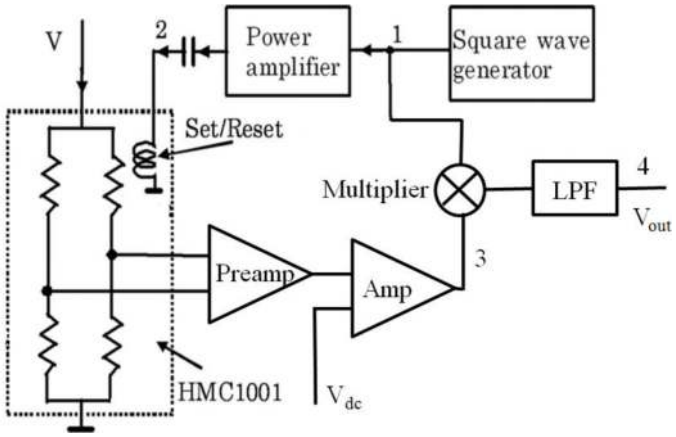

Figure 10. Block diagram of the AMR driving circuit with set/reset.

The pulse width was about 2 μs, which was the waveform 2 in **Figure 11**. The waveform 3 in **Figure 11** shows the output signal of the AMR bridge after a preamplifier with the gain of 40 dB. A multiplier was used to do the demodulation of the signal. After demodulation, a low-pass filter (LPF) with the cut-off frequency of 2 kHz was used and the waveform after the LPF was shown by waveform 4 in **Figure 11**.

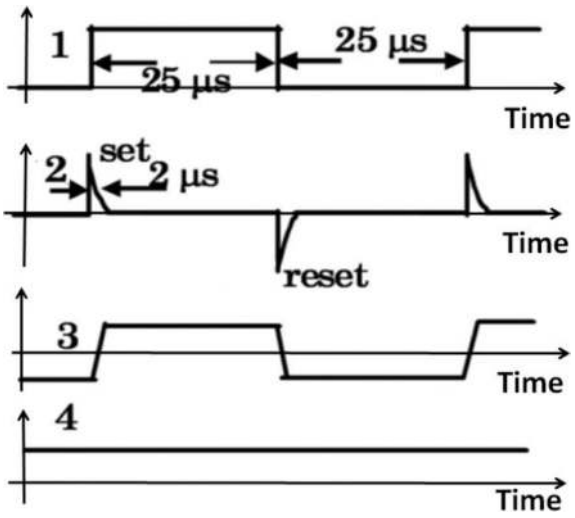

Figure 11. Waveforms of test point 1, 2, 3, and 4 in **Figure 10**.

We measured the output voltage signals for the AMR sensor with and without the Set/Reset method. The measurements were done in a magnetic shielded box. The measurement time was about 5 min with the measuring bandwidth from DC to 5 Hz. **Figure 12** shows the output

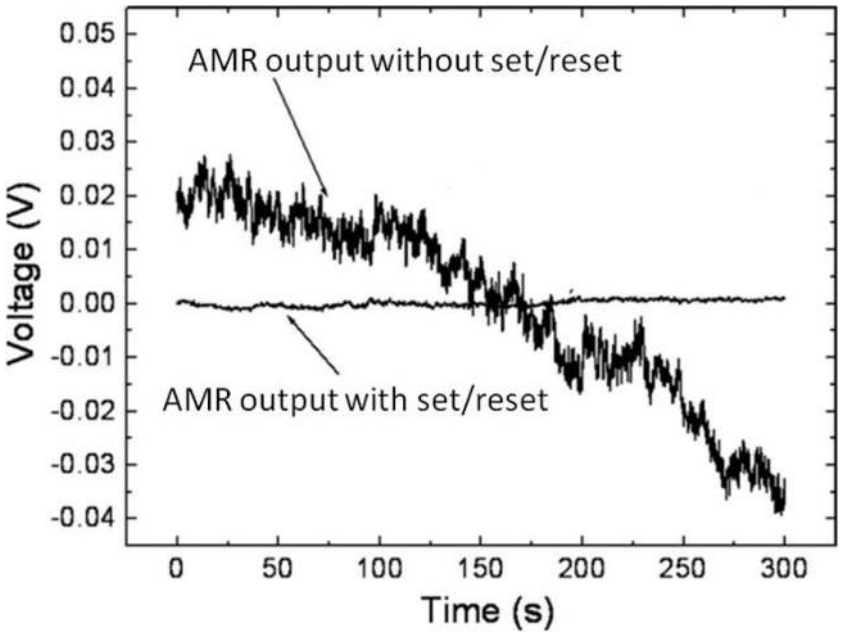

Figure 12. Output signal for the AMR sensor with Set/Reset and without Set/Reset.

signals. The total gains of the driving circuits for two methods were same. We observed that the output of the AMR sensor with the Set/Reset method was almost flat and the noise was smaller; however, the output without the Set/Reset method was not flat and the noise was bigger. The Set/Reset method was effective to reduce the influence of the variation of the temperature. Considering the total voltage/field transfer coefficient was about 6 mV/nT, the magnetic field resolution of the AMR sensor with the Set/Reset method was about 0.5 nT for the bandwidth from DC to 5 Hz.

3. Application to NDE

For the liquid rocket using liquid oxygen and liquid hydrogen, such as the H1-A rocket of Japan, the combustion chamber was made of Cu-Cr-Zr copper alloy (**Figure 13**). It was the ultra high temperature gas of about 3000 K inside of the combustion chamber. For cooling it, rectangular coolant passages were made in the wall of the cooper alloy and liquid hydrogen flew in them. With the very thin wall of 1 mm between the high temperature gas and the cooling liquid hydrogen, a big thermal gradient and an excessive thermal strain were generated in the inner wall of the combustion chamber. Due to the repeat of the oxidation/reduction, or the melting of the surface, some small cracks were generated. Now there was no effective method to detect the tiny defect in such complex structure. We were planning to detect the small defect in the copper alloy wall of combustion chamber using eddy current testing (ECT) with highly sensitive magnetic sensors.

We developed an ECT system using the AMR sensor and we successfully detected the artificial defects in plate-type samples [21, 22] and chamber-type samples [23], in which grooves and artificial defects were made to simulate the wall of the combustion chamber of a liquid fuel rocket. All experiments were done in an environment without shielding. **Figure 14** shows

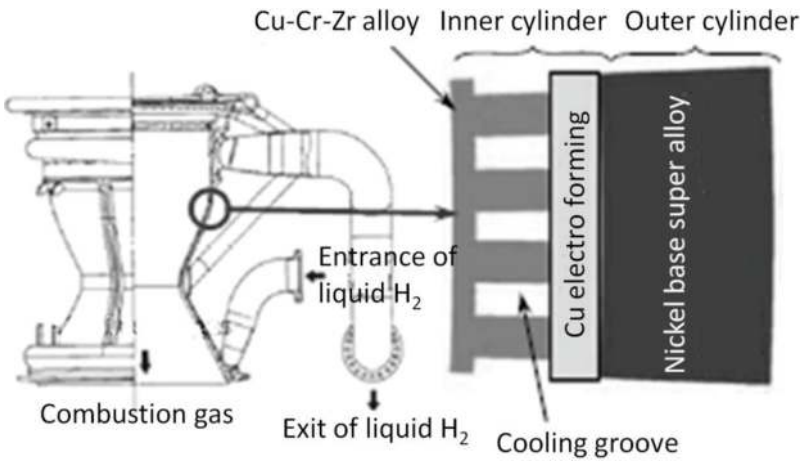

Figure 13. Combustion chamber of liquid rocket.

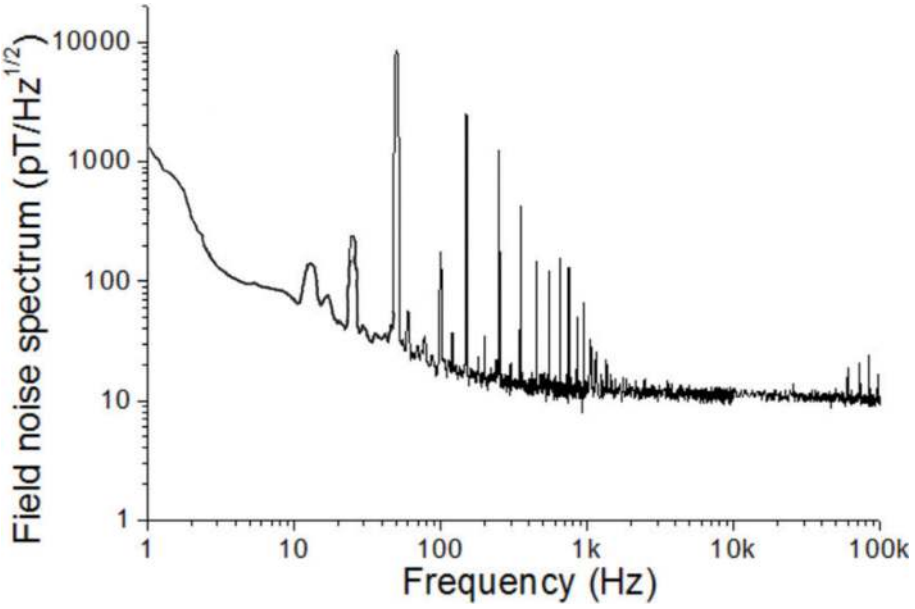

Figure 14. Magnetic field noise spectrum in our laboratory measured by AMR sensor.

the magnetic field noise spectrum measured in our laboratory using the AMR sensor. The peaks were 50 Hz interference and its harmonics.

First, we used an aluminium plate to simulate the complex structure of the inner wall of the liquid rocket combustion chamber. **Figure 15** shows the specimen. It was an aluminium plate with the size of 100 × 110 mm^2 and the thickness was 4 mm. Many parallel periodic ditches were made on one side of the aluminium plate. The depths of the ditches were 3 mm. The width of the ditches was 1 mm. Nine notches with different depths and lengths were made under the bottom of the ditches to simulate the defects of the combustion chamber.

Figure 16 shows the setup of the ECT system using the AMR sensor. The coil was used to produce the excitation field, and eddy current was induced in the specimen. The magnetic field produced by the eddy current was measured by the AMR sensor. The output signal of the AMR sensor was sent to a lock-in amplifier to get the amplitude signal or phase signal. The lock-in amplifier was also used to produce the sine signal sent to the excitation coil. In this AMR ECT system, the specimen was fixed on an X-Y stage. The movement of the X-Y stage was controlled by a computer. The movement resolution of the X-Y stage was about 50 μm, but the step of our measurement was set to 1 mm.

The excitation frequency was chosen according to the wall thickness between the scanning surface and the bottom of the notch. For the aluminium specimen, it was 1 mm, so 8 kHz was used, which had the penetration depth of about 1 mm. The current amplitude flow in the excitation coil was about 1 mA. The aluminium plate was fixed on the X-Y stage. The scanning was done over the backside of aluminium plate, where the ditches could not be seen. The scanning direction was perpendicular to the direction of crack.

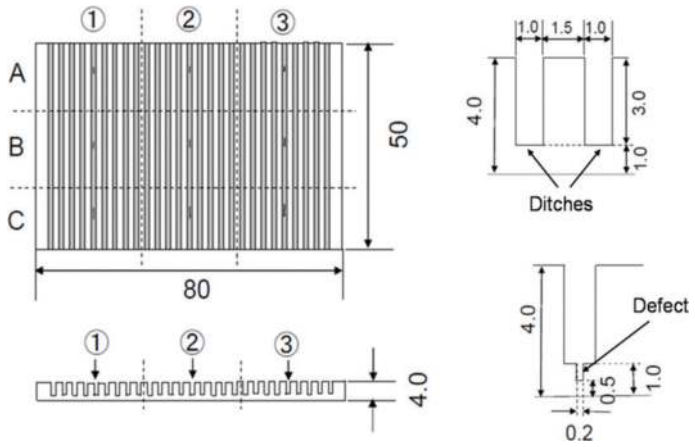

Figure 15. The aluminium specimen to simulate the combustion chamber and the defects. The depth and length of the notch defect under the bottom of some grooves: ①: depth of 0.25 mm. ②: depth of 0.5 mm. ③: depth of 0.75 mm. A: length of 2 mm. B: length of 5 mm. C: length of 10 mm.

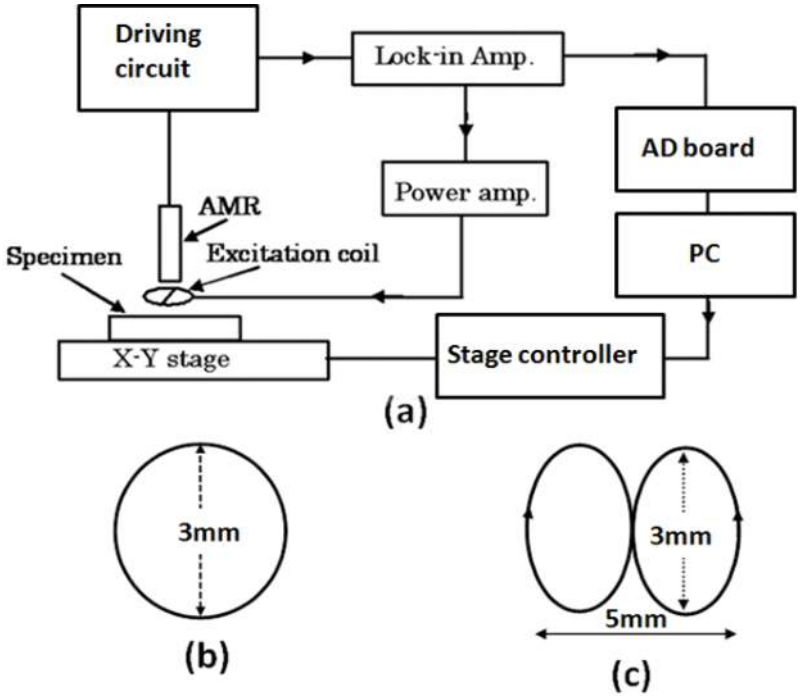

Figure 16. (a) The block diagram of the experimental setup of ECT using AMR sensor. (b) The circular excitation coil. (c) The double-D excitation coil.

Circular coil or differential coil, shown in **Figure 16(b)** and **(c)**, could be used as the excitation coil. When circular coil was used, the circular coil was 3 mm with 20 turns wound by 0.1 mm copper wire. The coil was attached to the bottom of the AMR sensor and the position of the coil was adjusted to make the output of the AMR biggest. When using circular coil, the strong background field was detected by the AMR sensor. When differential coil was used to produce the excitation field, the differential coil was 3 mm with 20 turns, which was attached to the bottom of the AMR sensor to produce the excitation field. When using differential coil, the background excitation field could be cancelled well. The position of the coil was adjusted to make sure that the AMR sensor had a smallest response to the excitation field. The other experimental conditions were same as that when using circular excitation coil.

Figure 17(a) shows the notch signals for one scanning using the circular coil, and **Figure 17(b)** shows the notch signals for one scanning using the differential coil. The signal-to-noise ratio was good for the cracks. **Figure 18** shows the 3D graph of the scanning results using the circular and **Figure 19** shows the 3D graph of the scanning results using the differential coil.

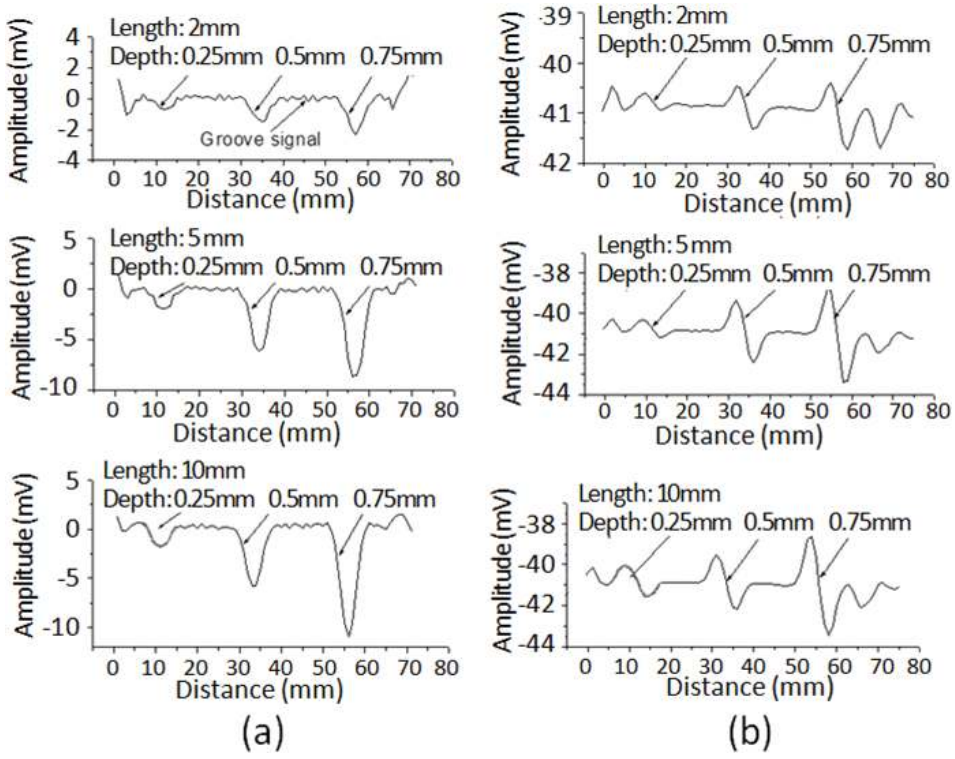

Figure 17. (a) The notch signal for one scanning when using circular excitation coil. (b) The notch signal for one scanning when using differential excitation coil.

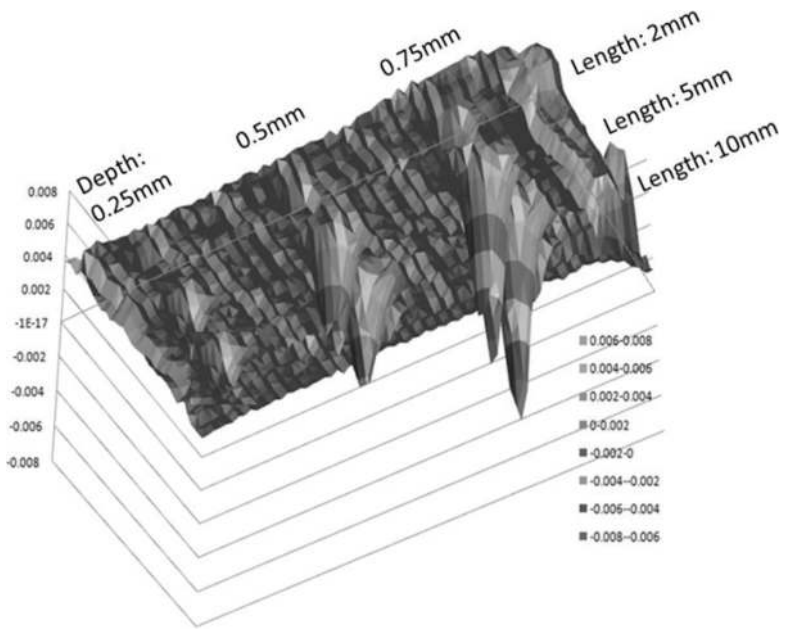

Figure 18. 3D graph of the results when using circular excitation coil.

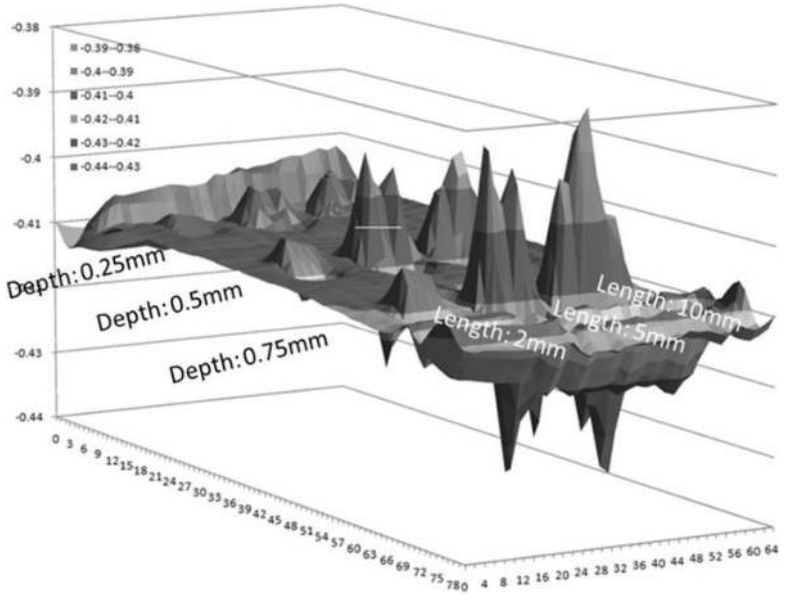

Figure 19. 3D graph of the results when using differential excitation coil.

We also prepared a chamber-type specimen made of copper alloy [23]. Grooves were fabricated to simulate the cooling grooves of the combustion chamber; and artificial notches were made under the bottoms of some grooves to simulate crack defects in the combustion chamber (**Figure 20**). The widths of the notches were about 0.3 mm. Notches with different lengths and depths were made. The lengths of the notches were 2, 5 and 10 mm, respectively; the remaining thickness of the wall at the positions of the notches was 0 mm (through), 0.2, 0.4 and 0.6 mm, respectively.

For chamber-type specimen, the lift-off variance during scanning might have a big influence to the output signals. Dual-frequency ECT [11, 23] was an effective method to reduce the influence of lift-off variance. **Figure 21** shows the schematic block diagram of the dual frequency ECT system with AMR sensor. The excitation coil was used to produce the AC magnetic field. Eddy currents were induced in the conductive specimen, and the AMR sensor was used to detect the magnetic field produced by the eddy currents. The sensing direction of the AMR sensor was along *Z* direction, which was perpendicular to the surface of the specimen. Two lock-in amplifiers and two frequencies were used in this ECT system. The amplitude output signal V_{f1} and V_{f2} of the two lock-in amplifiers were used and sent to a computer through an analog-to-digital (AD) board. Digital subtraction of V_{f1} and V_{f2} was done by the computer. The phase signals of the lock-in amplifiers were not used in our experiments.

The penetration depth of the applied AC magnetic fields could be estimated by the formula $\delta = (\pi f \mu \sigma)^{-1/2}$, where δ was the penetration depth, f was the frequency, μ was the magnetic permeability of the material and σ was the electrical conductivity of the material. For high frequency *f2*, the penetration depth was small, so mainly the surface roughness and variance of lift off were detected. For low frequency *f1*, the penetration depth was big; both the inside and surface properties of the material could be detected. If we subtracted the amplitude outputs (V1 and V2) of two lock-in amplifiers and choose a proper subtraction factor, it was possible to cancel the signals produced by the variance of liftoff during scanning.

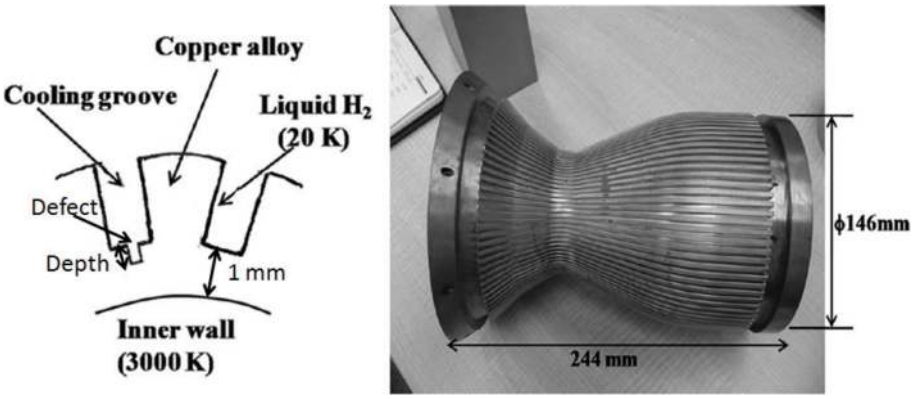

Figure 20. Chamber-type specimen to simulate the combustion chamber of liquid rocket.

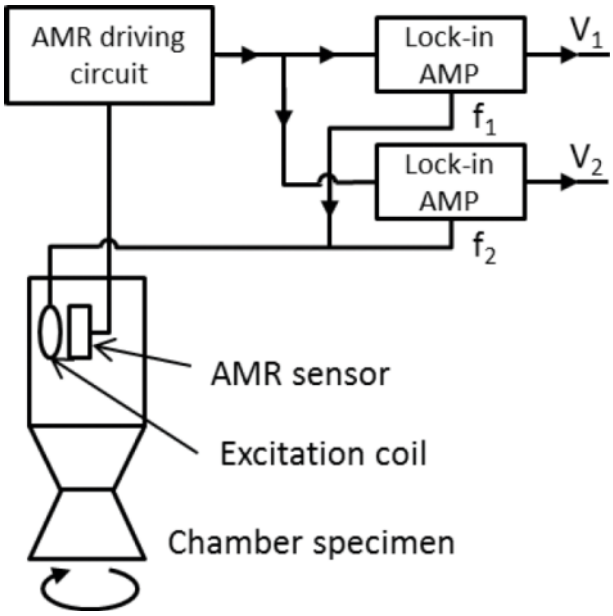

Figure 21. Dual frequency ECT system with AMR sensor.

The excitation coil was a 20 turn circular coil with an outer diameter of about 3 mm. The AMR sensor was located at the center of the excitation coil. The low frequency was 2 kHz and the high frequency was 20 kHz. The conductivity of the copper alloy was about 5×10^7 S/m. According to the wall thickness of the chamber (1 mm), 2 kHz was used as the low excitation frequency. The corresponding penetration depth was about 1.5 mm. The high excitation frequency was 20 kHz and the corresponding penetration depth was about 0.5 mm. The amplitude of the AC current flow in the excitation coil was about 10 mA. Scanning was realized by rotating the chamber with a motor. The rotating speed of the chamber was about 4 degree/s. The lift off between the surface of the specimen and the excitation coil was about 0.5 mm, and the variance of the lift off was about 0.2 mm during scanning.

Amplitude signals of the two lock-in amplifiers were used. **Figure 22** shows the scanning results for the notches with the remaining thicknesses of 0 mm (through) and 0.2 mm. Notches with the remaining thickness of 0 mm were detected by the low excitation frequency (2 kHz) and the high excitation frequency (20 kHz). For the notches with the remaining thickness of 0.2 mm, the signals became smaller for the high excitation frequency. During the scanning, the variance of the liftoff was about 0.2 mm, which causes the non-flatness of the lock-in amplifier output signals of $V_{2\,kHz}$ and $V_{20\,kHz}$. $V_{2\,kHz} - kV_{20\,kHz}$ was the subtraction result and k was a constant. For our experiments, when k = 0.46 was used, liftoff-related noise was compensated well. This proved that the dual frequency method was effective to reduce the influence of the variance of lift off.

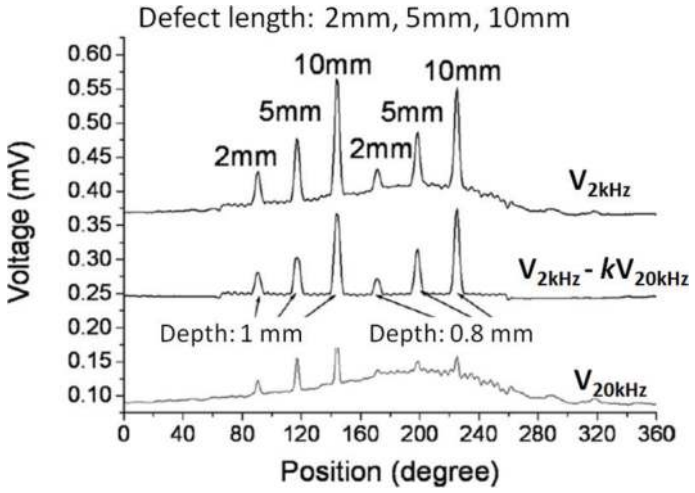

Figure 22. Scanning results for notches with the remaining wall thicknesses of 0 mm (through) and 0.2 mm.

Figure 23 shows the scanning results for the notches with the remaining wall thicknesses of 0.4 and 0.6 mm. For the low excitation frequency of 2 kHz, the defect signals could be obviously observed. For the high excitation frequency of 20 kHz, due to its small penetration depth, the notch signals were very small. Both the output signals of $V_{2\,kHz}$ and $V_{20\,kHz}$ were not flat, which was caused by the variance of the lift off during scanning. The subtraction result of $V_{2\,kHz}$–$kV_{20\,kHz}$ became flat, here k = 0.46 was also used. This also proved that the dual

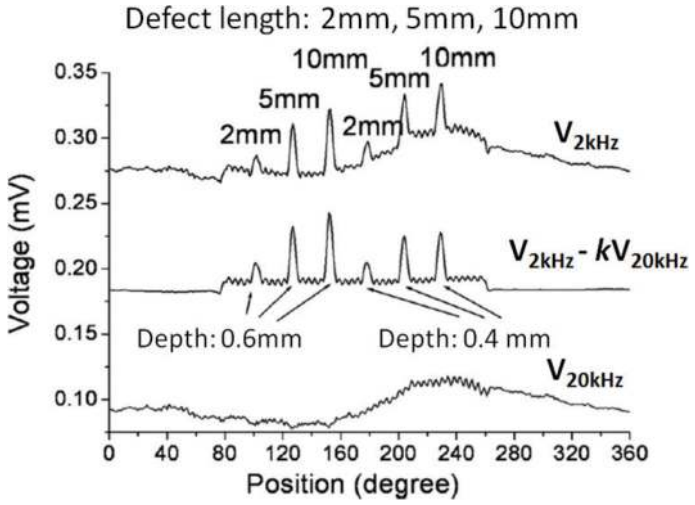

Figure 23. Scanning results for the notches with the remaining wall thicknesses of 0.4 and 0.6 mm.

frequency method was effective to reduce the influence of the variance of lift off. The small periodic signals were the signals produced by the grooves.

4. Conclusion

We improved the driving circuit of the AMR sensor. Using the commercial AMR sensor of HMC10001, lower magnetic field noise spectral densities of 12 pT/root(Hz) at 1 kHz and 20 pT/root(Hz) at 100 Hz were achieved. When the driving circuit operated at feedback mode, the distortion of the output was reduced. Using the Set/Reset method, the low frequency noise and the DC level drift caused by temperature effect were reduced. Using the optimized system of AMR sensor, we developed a high sensitive ECT NDE system and the small defects in the combustion chamber of liquid rocket were successfully detected.

Acknowledgements

We thank the helps from Dr M. Shiwa and Dr S. Moriya.

Author details

Dongfeng He

Address all correspondence to: he.dongfeng@nims.go.jp

National Institute for Materials Science, Tsukuba, Japan

References

[1] Tumanski S. Induction coil sensors—A review. Measurement Science and Technology. 2007;**18**:R31-R46

[2] Park DG, Angani CS, Rao BPC, Vertesy G, Lee DH, Kim KH. Detection of the subsurface cracks in a stainless steel plate using pulsed eddy current. Journal of Nondestructive Evaluation. 2013;**32**:350-353

[3] Bernieri A, Betta G, Ferrigno L, Laracca M. Improving performance of GMR sensors. IEEE Sensors Journal. 2013;**13**:4513-4521

[4] Betta G, Ferrigno L, Laracca M. GMR-based ECT instrument for detection and characterization of crack on a planar specimen: a hand-held solution. IEEE Transactions on Instrumentation and Measurement. 2012;**61**:505-512

[5] Jander A, Smith C, Schneider R. Magnetoresistive sensors for nondestructive evaluation. In: Conference on Advanced Sensor Technologies for Nondestructive Evaluation and Structural Health Monitoring; 8-10 March 2005; San Diego, CA. Proceedings of the Society of Photo-Optical Instrumentation Engineers (SPIE). Vol. 5770. 2005. pp. 1-13

[6] Allweins K, von Kreutzbruck M, Gierelt G. Defect detection in aluminium laser welds using an anisotropic magnetoresistive sensor array. Journal of Applied Physics. 2005;**97**:10Q102. DOI: 10.1063/1.1852391

[7] Koch RH, Rozen JR. Low-noise flux-gate magnetic-field sensors using ring and rod-core geometries. Applied Physics Letters. 2001;**78**:1897-1899

[8] Fujita Y, Sasada I. Detection of flaws in ferromagnetic samples based on low frequency eddy current imaging. Journal of Applied Physics. 2003;**93**:8277-8279

[9] He DF, Daibo M, Yoshizawa M. Mobile HTS rf SQUID magnetometer. IEEE Transactions on Applied Superconductivity. 2003;**13**:200-202

[10] Tavrin Y, krause HJ, Wolf W, Glyantsev V, Schubert J, Zander W, Bousack H. Eddy current technique with high temperature SQUID for non-destructive evaluation of non-magnetic metallic structures. Cryogenics. 1996;**36**:83-86

[11] He DF, Yoshizawa M. Dual-frequency eddy-current NDE based on high-T-c rf SQUID. Physica C: Superconductivity and Its Applications 2002;**383**:223-226

[12] Stutzke NA, Russek SE, Pappas DP. Low-frequency noise measurements on commercial magnetoresistive magnetic field sensors. Journal of Applied Physics. 2005;**97**:10Q107. DOI: 10.1063/1.1861375

[13] He DF, Tachiki M, Itozaki H. Highly sensitive anisotropic magnetoresistance magnetometer for eddy-current nondestructive evaluation. Review of Scientific Instruments. 2009;**80**:036102. DOI: 10.1063/1.3098946

[14] Thomson W. On the electrodynamic qualities of metals: Effects of magnetization on the electric conductivity of nickel and iron. Proceedings of the Royal Society of London. 1857;**8**:546-550

[15] McGuire TR, Potter RI. Anisotropic magnetoresistance in ferromagnetic 3D alloys. IEEE Transactions on Magnetics. 1975;**11**:1018-1037

[16] Kuijk KE, Vangestel WJ, Gorter FW. Barber pole, a linear magnetoresistive head. IEEE Transactions on Magnetics. 1975;**11**:1215-1217. DOI: 10.1109/TMAG.1975.1058886

[17] The Datasheet of HMC1001. Honeywell International Inc, https://aerospace.honeywell.com/en/~/media/aerospace/files/datasheet/1and2axismagneticsensorshmc1001-1002-1021-1022_ds.pdf

[18] West FG. Magnetoresistive measurements on domain rotation nickel-iron alloy films. Nature. 1960;**188**:129-130

[19] He DF, Jia JP. Heat transfer effects in scanning anisotropic magnetoresistive imaging. IEEE Transactions on Magnetics. 2011;**47**:264-266. DOI: 10.1109/TMAG.2010.2088131

[20] He DF, Shiwa M. An anisotropic magneto resistive sensor with set/reset field. Review of Scientific Instruments. 2011;**82**:094703. DOI: 10.1063/1.3640412

[21] He DF, Shiwa M, Uetake I, Yamawaki H, Tachiki M, Itozaki H. Basic examination for the defect detection of combustion chamber using ECT with AMR sensor. Journal of JSNDI. 2010;**59**:510-514

[22] He DF, Shiwa M, Jia JP, Takatsubo J, Moriya S. Multi-frequency ECT with AMR sensor. NDT & E International. 2011;**44**:438-441. DOI: 10.1016/j.ndteint.2011.04.004

[23] He DF, Zhang YZ, Shiwa M, Moriya S. Development of eddy current testing system for inspection of combustion chambers of liquid rocket engines. Review of Scientific Instruments. 2013;**84**:014701. DOI: 10.1063/1.4773539